Influence of the pore size and porosity of selective laser melted Ti6Al4V ELI porous scaffold on cell proliferation, osteogenesis and bone ingrowth

Ziyu Chen, Xingchen Yan, Shuo Yin, Liangliang Liu, Xin Liu, Guorui Zhao, Wenyou Ma, Weizhong Qi, Zhongming Ren, Hanlin Liao, et al.

Influence of the pore size and porosity of selective laser melted Ti6Al4V ELI porous scaffold on cell proliferation, osteogenesis and bone ingrowth

Ziyu Chen [1,3,4#], Xingchen Yan [2,5#*], Shuo Yin [7], Liangliang Liu [1,3,4#], Xin Liu [1,3,4], Guorui Zhao [2], Wenyou Ma [2], Weizhong Qi [1,3,4], Zhongming Ren [6], Hanlin Liao [5], Min Liu [2,*], Daozhang Cai [1,3,4*], Hang Fang [1,3,4*]

1. Department of Orthopedics, The Third Affiliated Hospital of Southern Medical University, No.183, Zhongshan West Avenue, Tianhe District, Guangzhou 510630, Guangdong, P.R. China
2. National Engineering Laboratory for Modern Materials Surface Engineering Technology; The Key Lab of Guangdong for Modern Surface Engineering Technology; Guangdong Institute of New Materials, Guangzhou 510651, P.R. China
3. Academy of Orthopedics, Guangdong Province, P.R. China
4. Orthopedic Hospital of Guangdong Province, P.R. China
5. ICB UMR 6303, CNRS, Univ. Bourgogne Franche-Comté, UTBM, F-90010 Belfort, France
6. Shanghai University & State Key Laboratory of Advanced Special Steel, Shanghai 200072, P.R. China
7. Trinity College Dublin, The University of Dublin, Department of Mechanical and Manufacturing Engineering, Parsons Building, Dublin 2, Ireland

Abstract: This paper systematically investigates the biomedical performance of selective laser melted (SLM) porous Ti6Al4V ELI scaffolds for bone implantation through *in vitro* and *in vivo* experiments. Scaffolds with pore sizes of 500 μm, 600 μm and 700 μm and porosities of 60% and 70% were manufactured in order to explore the optimum pore size and porosity. Rat bone marrow mesenchymal stem cells (rBMMSCs) were used in the *in vitro* experiments. Cell Counting Kit-8, live/dead staining and scanning electron microscope were used to assess the cytotoxicity of the porous scaffolds. DNA content quantification was performed to investigate cell proliferation on the porous scaffolds. The osteogenic differentiation of cells was measured by alkaline phosphatase (ALP) activity and osteogenic gene expressions, including bone morphogenetic protein-2 (BMP-2), collagen type 1α1 (COL-1), osteocalcin (OCN), osteopontin (OPN) and runt-related transcription factor-2 (RUNX-2). The Sprague-Dawley (SD) rat models with distal femoral condyles defect were used in the *in vivo* experiments. Micro-CT analysis and histological analysis were performed after implantation surgery to reveal the bone ingrowth into the porous scaffolds. All *in vitro* data were analyzed by one-way ANOVA followed by Tukey post hoc tests, *in vivo* data were analyzed using Kruskall-Wallis ANOVA and Conover-Inman post-hoc test. Based on the *in vitro* and *in vivo* experiments, it is found that the porous scaffolds manufactured by SLM did not induce a cytotoxic effect. Among all the porous scaffolds, the scaffold with a pore size of 500 μm and porosity of 60% showed the best cell proliferation and osteogenic differentiation (*in vitro* experiments) and bone ingrowth (*in vivo* experiments).

# These authors contribute equally to this work: Ziyu Chen, Xingchen Yan, Liangliang Liu

* Corresponding authors: Xingchen Yan (xingchen.yan@utbm.fr); Min Liu (liumin@gdas.gd.cn); Daozhang Cai (cdz@smu.edu.cn); Hang Fang (fanghang@smu.edu.cn)

Keywords: bone defect; pore size; porosity; Ti6Al4V ELI; osteogenesis; bone ingrowth

1 Introduction

Arthroplasty is an effective treatment of arthropathy as it can relieve pains, restore physical activities, and improve life quality of patients. Over the past 20 years, there was a considerable increase in the number of patients in the world who underwent arthroplasty. More than 800,000 patients receive primary arthroplasty every year with an annual growth rate of 20% [1]. However, the service life of an artificial joint prosthesis is normally limited due to the occurrence of aseptic loosening, joint instability and infection, and revision of previous arthroplasty is required. Many difficult issues may inevitably arise during the revision surgery, of which osseous defects are the most intractable situation [2]. Currently, the treatment of large or non-healing bone defects is generally performed with autografts or allografts. Despite regarded as the "golden standard" for repairing bone defects, autologous bone graft also encounters drawbacks. Donor site complications is a typical drawback of autologous bone graft. Allogeneic bone transplantation may cause immune rejection and disease transmission, which significantly harm the health of patients. Therefore, in recent years, synthetic alternatives are becoming a practicable and fascinating option [3].

Bio-ceramic bone implant is a bone graft substitute, consisting of calcium and phosphates, demonstrating good bioactivity and biodegradation properties. However, as degradation gradually occurs, the reduction of the mechanical properties of the implant may bring potential risks to the recovery. Alternatively, implant made by metals is another option for bone graft substitute. However, metal implants naturally have much higher elastic modulus (e.g. 100–140 GPa for Ti alloys [4], 210–253 GPa for Co alloys [5] and 190–210 GPa for stainless steel [6]) than bone tissues (0.5–20 GPa) [7]. Such incompatible elastic modulus may lead to implant loosening or autogenous bone fracture. Due to the inferior biomechanical compatibility of the traditional metallic implants, the interfacial adhesion between the hard tissues and the implant is unstable. Porous structure has been recognized as an effective way to eliminate this mismatch of elastic modulus [8]. By adjusting pore size and porosity, an ideal metal implant with optimized density, strength and mechanical compatibility with the bone tissues can be achieved, which can effectively prevent osteonecrosis and osteogenesis deformity around the implant [9, 10]. In addition, the internal perforated porous structure is beneficial to the adhesion, proliferation and differentiation of mesenchymal stem cells. The porous structure also provides high interfacial bond area for vascularization and bone ingrowth [11], promoting the biological fixation of implants and bones.

Conventional manufacturing technologies for porous metals include powder sintering, deposition, and chemical reaction. However, due to the technological limitations, these methods generally bring undesirable properties to the implants. Powder sintering results in inferior mechanical properties of the implants due to the existence of residual defects. Deposition method suffers from a slow sedimentation rate and a high production cost. Chemical reaction cannot

accurately control pore size and porosity distribution, which is crucial to porous implants [12]. Therefore, considering the limitations of the aforementioned technologies, a promising manufacturing process with high controllability and repeatability for producing reliable mechanical and morphological properties of porous implants is urgently needed [13].

Selective laser melting (SLM) as a novel additive manufacturing technique has drawn increasing attention from both industrial and medical communities. With the assistance of computer-aided design (CAD), successive and selective powder bed fusion can be achieved through a high-energy laser beam [14, 15]. The SLM scaffold is then fabricated via the rapid solidification and the thin welding between each deposited layer. Due to the high freedom in complex geometry design, SLM can be used in the production of porous implants [16] by tailoring their pore size and porosity to satisfy specific requirements of different individuals [17, 18]. Recently, it has been reported that this technology can manufacture porous implants with profitable mechanical and biological properties [19-21]. Among all the relevant studies, there are few works concerning the effect of porosity and pore size on the mechanical and biological properties of SLM implants.

Fuduka et al. [19] studied the osteoinduction of SLM Ti implants with a channel structure. In these works, significant osteoinduction was observed when the pore sizes were 500 and 600 μm. Wauthle et al. [12] investigated the SLM dodecahedron porous pure Ta implants with the average pore size about 500 μm and porosity of 80 %. The *in vivo* test showed favorable biocompatibility of the SLM Ta implants and a yield strength of 12.7 MPa. Wally et al. [22] analyzed the role of the pore size of SLM Ti6Al4V porous structure in dental applications. However, no decisive conclusions were drawn due to the lack of regularity between the pore structure and osteointegration. Taniguchi et al. [2] reported that the SLM porous Ti6Al4V implant with a designated porosity of 65% and a pore size of 600 μm had more comparable mechanical strength with the bone, higher fixation ability and more bone ingrowth than those with a pore size of 300 and 900 μm. Moreover, based on a well-designed experiment, Wieding et al. [23] concluded that the SLM porous Ti6Al4V scaffold with a pore size of 700 μm could stabilize segmental bone defects in the metatarsus of sheep. In addition to the aforementioned SLM porous Ti-based implants, the porosity and pore size of diffusion bonded porous Ti were also studied by Li et al. [24] and Chang et al. [25]. It was reported that the porous Ti with a porosity of 60-70% could greatly match the human trabecular bone in terms of mechanical properties. Furthermore, the porous Ti with a porosity of 70% and a pore size of 313 μm and 390 μm exhibited the best cell proliferation and bone ingrowth capability. However, it is worth noting that the surface of diffusion bonded porous meshes is much smoother than that of SLM porous structure. Hence, they may have different responses to cells.

Despite having a number of investigations, the optimum porosity and pore size of implants for bone ingrowth,

particularly the SLM porous implants, is still not well understood. A systematic investigation on the effect of the porosity and pore size of SLM porous scaffolds on the mechanical and biological properties is urgently needed in order to improve the reliability and safety of SLM porous scaffolds in medical applications. Therefore, the aim of this work is to explore the optimum porous structure in terms of porosity and pore size of a SLM Ti6Al4V ELI scaffold for biomedical implant. In order to achieve this objective, various scaffolds with pore sizes of 500, 600 and 700 μm and porosities of 60% and 70% were manufactured by SLM. Elaborate *in vitro* and *in vivo* experiments were then conducted to evaluate the biological performance of the porous scaffolds.

2 Experimental details

2.1 Feedstock materials

Ti6Al4V ELI (Extra Low Interstitials, Grade 23) is known to have excellent mechanical and biological properties [8, 26] than other Ti alloys. As compared to Ti6Al4V (Grade 5), Ti6Al4V ELI contains lower levels of oxygen, nitrogen, carbon and iron than, exhibiting better ductility and improved fracture toughness. Considering the superior biological properties of Ti6Al4V ELI, gas atomized spherical Ti6Al4V ELI powder (EOS GmbH, Germany) was supplied as feedstock in this work. The size range of the powder is measured to be 22-51 μm by a laser particle sizer (Mastersizer 2000, Malvern Instruments Ltd., UK). The chemical composition of the Ti6Al4V ELI provided by supplier is listed in Table. 1.

Table. 1. Chemical composition of the Ti6Al4V ELI powder used in this work

Element	Ti	Al	V	O	N	C	H	Fe
wt.%	Balance	5.5-6.5	3.5-4.5	<0.13	<0.03	<0.08	<0.012	<0.25

2.2 Design and manufacture of porous Ti6Al4V ELI scaffolds

Detailed information of the SLM Ti6Al4V ELI porous scaffolds used in this work is provided in Fig.1. Octahedron crystal lattice with horizontal struts was adapted as the basic unit of the porous structure as shown in Fig. 1a. The overhanging cuboid strut has an inclined angle of 45°. The octahedron lattice can improve the isotropic properties of the structure under multidirectional compressive force and hence confers high safety as the bone substitute. The structure of the scaffolds was designed using CAD software UG NX 10 (Siemens PLM Software, Germany). Fig. 1b and 1c show the CAD-designed porous Ti6Al4V ELI scaffolds in flat shape (10 mm × 10 mm × 2 mm, layer thickness of 2 mm) for *in vitro* experiments and in cylindrical shape (3 mm in diameter and 4 mm in length) for *in vitro* experiments, respectively.

By referring the previous works and considering the processing accuracy of the SLM machine used in this work, the scaffolds were designed to have porosities of 60% and 70%, and pore sizes of 500, 600 and 700 μm. For the convenience of the following result demonstration and discussion, the scaffolds with a porosity of 60% and pore sizes of 500, 600 and 700 μm were annotated as A500, A600 and A700, respectively. Similarly, the scaffolds with a porosity of 70% and pore sizes of 500, 600 and 700 μm were annotated as B500, B600 and B700, respectively. For emphasizing the advantages of the porous scaffolds, a solid plate (10 mm × 10 mm × 2 mm) was also manufactured by SLM and compared with the porous scaffolds in the *in vitro* experiments. As a reference, the solid plate was annotated as REF1.

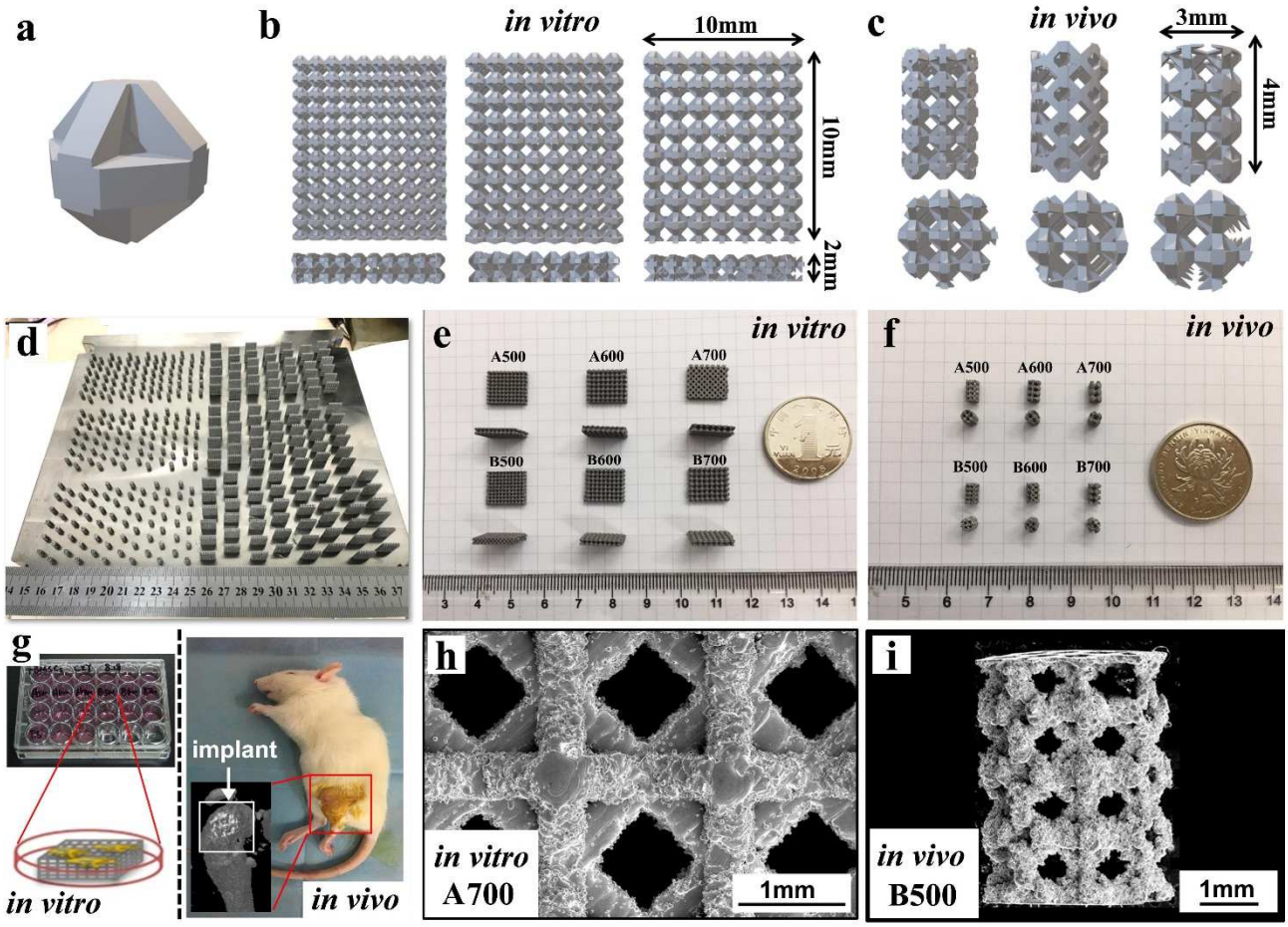

Fig. 1. Design and manufacture of the Ti6Al4V ELI porous scaffolds (a) A single octahedral cell, (b) CAD-designed porous Ti6Al4V ELI scaffolds in flat shape (10 mm × 10 mm × 2 mm, layer thickness of 2 mm) for *in vitro* experiments, (c) CAD-designed porous Ti6Al4V ELI scaffolds in cylindrical shape (3 mm in diameter and length 4 mm in length) for *in vivo* experiments, (d) photo of the as-fabricated Ti6Al4V ELI scaffolds on a Ti substrate, (e) high-magnification photo of the scaffolds for *in vitro* experiments, (f) high-magnification photos of the scaffolds for *in vivo* experiments, (g) schematic of the *in vitro* and *in vivo* experiments, (h) SME image of A700 scaffold used for *in vitro* experiments (i) SME image of B500 used for *in vivo* scaffold experiments.

EOS M290 system (EOS GmbH Germany) was used to produce Ti6Al4V ELI scaffolds. The system is equipped with an Yb-Fiber laser (1064 nm) with a spot size of 100 μm. Optimized manufacturing parameters were applied in the experiments with a laser power of 240 W, a scanning speed of 240 mm/s, a layer thickness of 30 μm and a hatch distance

of 50 μm [27, 28]. Fig. 1d shows the photo of the as-fabricated SLM Ti6Al4V ELI scaffolds on a Ti substrate. The high-magnification photos of the scaffolds for *in vitro* and *in vivo* experiments are shown in Fig. 1e and f, respectively.

Fig. 1g shows the schematic of the *in vitro* and *in vivo* experiments. rBMMSCs were used to investigate the cytotoxicity and proliferation and osteogenic differentiation of the cells on the porous scaffolds. The rat model with distal femoral condyles defect were used to investigate the effect of bone ingrowth into the porous scaffolds. Fig. 1h and i show the scanning electron microscope (SEM, FEI Nova NanoSEM 450) images of A700 scaffold used for *in vitro* experiments and B500 scaffold used for *in vivo* experiments, respectively. It can be seen that the waviness and staircase on the strut surfaces slightly reduce the dimensional accuracy of the SLM porous scaffolds as compared to the original CAD design (Fig. 1b and c), which has also been reported in previous work [8, 29].

2.3 Porous scaffolds preparation, water contact angle, protein adsorption

The porous Ti6Al4V ELI scaffolds were ultrasonically cleaned in ethanol and double distilled water for 15 minutes, dried in a furnace at 65 °C for 1 hour and sterilized in an autoclave (120 °C for 20 minutes) before they were used in *in vitro* and *in vivo* studies. Water contact angles of the scaffolds were measured by a contact angle goniometer (KRUSS, Germany). Liquid droplet was dropped vertically onto the surface in the central area of scaffolds and the shape of the liquid drop (diameter about 2.3 mm) was captured by a camera and analyzed using the corresponding software (n = 3). For protein adsorption study, the porous scaffolds (n = 3) were put into 500 μL 1 g/L bovine serum albumin (fraction V, Germany) solution prepared from phosphate buffer saline (PBS, pH 7.4) in a 24-well plate. After incubation for 1 hour and 24 hours at 37 °C, the scaffolds were carefully washed by PBS and 500 μL 2% sodium dodecyl sulfate solution prepared from PBS was used to elute the adsorbed proteins. BCA Protein Assay Kit (Beyotime, Haimen, China) was used to estimate the adsorbed protein concentration. The absorbance was measured using a microplate absorbance reader (synergy HTX multi-mode reader, USA) at 562 nm.

2.4 Isolation and culture of rat bone marrow mesenchymal stem cells

The Sprague-Dawley (SD) rats were purchased from the Animal Experimental Center of Southern Medical University. All procedures were performed in accordance with the guidelines of the University Research Ethics Committee of Southern Medical University. rBMMSCs were obtained from the bone marrow of two-week-old rats, as reported previously [30]. Specifically, both femurs and tibias were aseptically dissected after the euthanasia of the rats. The bone marrow contents were flushed out from the diaphysis with minimal essential medium alpha basic (α-MEM,

Gibco, USA), collected by centrifuging, resuspended in a growth medium containing α-MEM, 10% (v/v) fetal bovine serum (FBS, Gibco, USA) and antibiotics (100 unit/mL penicillin, 100 μg/mL streptomycin; Gibco, USA), and cultured in a humidified atmosphere with 5% CO_2 at 35 °C. The medium was refreshed every 3 days. When the adherent cells grew to about 80% confluence, the rBMMSCs were passaged with 0.25% trypsin (Sigma, USA). The cells of passage 2 were used in the experiments. The rBMMSCs were seeded directly onto the scaffolds in the 24-well plates (Nest, USA) at a density of 5×10^4 cells per well and cultured for 1 day. Then, the scaffolds were moved to new 24-well plates to discard cells that adhered to the plate rather than to the scaffolds.

2.5 *In vitro* cytotoxicity and cell proliferation

In vitro cell cytotoxicity effects of the porous scaffolds, in accordance with ISO 10993-5, were analyzed on the rBMMSCs. Liquid extracts of the scaffolds (3 cm^2/mL in α-MEM with 10% FBS (v/v) at 37 °C) over 3 days were prepared and filter sterilized before utilized in cell cytotoxicity assays, which were assessed using Cell Counting Kit-8 (CCK-8). The rBMMSCs were seeded into 96-well plates (Nest, USA) at 1×10^4 cells per well for 1 day, then the culture medium was replaced by liquid extracts of medical grade polyethylene (negative control, NC, non-cytotoxic), α-MEM with 10% FBS (v/v) and 10% dimethyl sulfoxide (DMSO) (positive control, provide reproducible cytotoxic response), and the 100% liquid extracts of the Ti6Al4V ELI scaffolds from each group (100 μL/well) for a further 1, 3 and 5 days (n = 6). Following this, 10 μL of CCK-8 solution was added to each well of the plate and the plate was incubated without light for 2 hours. The absorbance at 450 nm was measured. The values of NC wells were averaged and taken as 100% cell survival. All other values were then averaged with respect to their groups and compared to the negative control. Moreover, after the cells were seeded onto the scaffolds and cultured for 1 and 7 days, live/dead staining was performed in accordance with the manufacturer's instruction. SEM was used to visualize the morphology of cells on the porous scaffolds after culture for 1 day.

Transfected with a lentiviral construct containing a green fluorescent protein (GFP) (cyagen, RASMX-01101, USA) expression motif, the rBMMSCs expressing GFP were used for cell proliferation assessment. The fluorescent images of cells on the scaffolds with different porosities and pore sizes were captured by an inverted fluorescence microscope (Olympus, Japan) after cultured for 1, 4, 7, 11, 14 and 21 days. DNA contents measurement were performed using Quant-iT PicoGreen dsDNA Assay Kit (Invitrogen, California, USA) to quantitatively assess the proliferation of the cells.

2.6 Alkaline phosphatase (ALP) activity and relative gene expression

The osteogenic differentiation was measured by ALP activity and osteogenic related genes expression. At day 7, 14 and 21, the ALP levels of the cells on the scaffolds were assessed using an alkaline phosphatase colorimetric assay kit (Beyotime, China) (n = 3) and normalized by the total protein contents which were measured by a BCA protein assay kit. The expression levels of osteogenic genes including bone morphogenetic protein-2 (BMP-2), collagen type 1α1 (COL-1), osteocalcin (OCN), osteopontin (OPN) and runt-related transcription factor-2 (RUNX-2) were evaluated by quantitative real-time PCR at day 7, 14 and 21. Specifically, the total RNA was extracted using Trizol reagent (Invitrogen, USA) and converted to cDNA using a HiScript II Q RT SuperMix (Vazyme, Nanjing, China). Then, the analysis was performed with ChamQ SYBR qPCR Master Mix (Vazyme, China) using the Roche Applied Science Light Cycler 96 system (Roche Applied Science, Penzberg, Germany) (n = 3). The relative expression levels of the osteogenic genes were standardized to the housekeeping gene glyceraldehyde-3-phosphate dehydrogenase (GAPDH). The synthesized primers employed in this study are listed in Table. 2.

Table. 2. Primers used in real-time PCR

Gene		Primer sequence (5'-3')	
		Forward	Reverse
GAPDH	Housekeeping	GGCACAGTCAAGGCTGAGAATG	ATGGTGGTGAAGACGCCAGTA
BMP-2	Osteogenic	CAACACCGTGCTCAGCTTCC	TTCCCACTCATTTCTGAAAGTTCC
COL-1	Osteogenic	GCCTCCCAGAACATCACCTA	GCAGGGACTTCTTGAGGTTG
OCN	Osteogenic	ATGAGAGCCCTCACACTCCTC	GCCGTAGAAGCGCCGATAGGC
OPN	Osteogenic	ACAAGCAGACGTTTTGACTC	CTTTGACCTCAGTCCGTAAG
RUNX-2	Osteogenic	CCATAACGGTCTTCACAAATCCT	TCTGTCTGTGCCTTCTTGGTTC

Abbreviations: GAPDH, glyceraldehyde-3-phosphate dehydrogenase; BMP-2, bone morphogenetic protein-2; COL-1, collagen type 1α1; OCN, osteocalcin; OPN, osteopontin; RUNX-2, runt-related transcription factor-2.

2.7 Surgical procedures

According to international standards, the *in vivo* experiment was approved by the Laboratory Animal Care & Welfare Committee of Southern Medical University. 10-week-old SD rats (n = 84) with body weight in the range of 350–400 g were used in this study. All rats were fed with a standard diet separately in polypropylene cages in the laboratory animal house at 20–25 °C under 50–55% humidity. All rats were randomly allocated to two time points (4 and 12 weeks). At each time point, the rats were randomly divided into seven groups (n = 6). General anesthesia was implemented with intraperitoneal injection of 1% pentobarbital sodium (6 mL/kg). Local anesthesia was implemented with a solution of 0.5%

lidocaine (0.2 mL/rat). The drilling of bone defects was conducted using a drill with a diameter of 3 mm, under the irrigation of physiological saline. The cylindrical porous implants (Fig. 1i) were inserted into the drilled holes at the distal lateral femoral condyle of the left hind leg. Then, the incisions were closed in a layered fashion with 6-0 absorbable catgut suture for muscles and 4-0 non-absorbable suture for the skin. Subcutaneous implantation was also made under the back skin of the rats to observe soft tissues ingrowth. For comparison, in the reference group (annotated as REF2), the bond defects were not repaired, and incisions were closed without any implantations. Cephazolin (10 mg/kg) was administered intramuscularly immediately after the suture and once a day for 3 days after the surgery. After 4 and 12 weeks of implantation, the rats were euthanized by injecting an overdose of pentobarbital sodium, and specimens containing the scaffolds were retrieved and fixed in 4% paraformaldehyde for 24 hours for further studies.

2.8 Micro-CT assay

In order to evaluate the effectiveness of new bone ingrowth formation, the rats with porous scaffold implantation were scanned using X-ray micro computed tomography (μ-CT, X5000, North Star Imaging, USA). The scanning resolution was approximately 4 μm/voxel. Three-dimensional (3D) volume of the scaffolds and bones were reconstructed by Amira-Avizo software. VGStudio MAX (Volume Graphics, Germany) was used for data analysis. The scaffolds and the bone tissues growing into the inner space of the scaffolds were defined as the volume of interest for detailed data analysis. Bone volume (BV) and total pore volume (TV) were measured using the μ-CT. The ratio of BV to TV (BV/TV) was then calculated to quantitatively evaluate the bone ingrowth performance. A higher value of BV/TV indicates better bone growth into the pore space. Note that TV in the reference group (REF2) equals to the volume of the entire bone defect.

2.9 Histological evaluation

After fixation for 1 day, the dehydration process of the specimens was done by a graded ethanol series. Then the specimens were embedded in methyl methacrylate solution at 37 °C for 1 week. Polymerized blocks were cut into thin sections (approximately 100 μm in thickness) along the perpendicular direction towards the long axis of the scaffolds, using an interlocked diamond saw (Leica Microtome, Germany). To investigate bone ingrowth into the porous scaffolds, Van-Gieson staining (1.2% trinitrophenol and 1% acid fuchsin) was performed on the sections.

2.10 Statistical analysis

All results in this study were retrieved from at least 3 independent experiments on at least three different samples, and expressed as the means ± standard deviations (SDs). Error bars in the charts represent SDs. Statistical analyses for *in*

vitro studies were done using one-way ANOVA and Tukey post hoc tests, and that for *in vivo* studies were done using Kruskall-Wallis ANOVA and Conover-Inman post-hoc test, while $p < 0.05$ indicates statistically significant.

3 Results

3.1 Water contact angle and protein adsorption

The image of water droplets and measured contact angle of the scaffolds are shown in Fig. 2a and b. As can be seen, all scaffolds exhibited a water contact angle of smaller than 90°. The water contact angle gradually decreased as the pore size increased. Porosity seemed to have no significant influence on the water contact angle; increasing porosity only slightly reduced water contact angle. As compared with REF1, A500 and B500 scaffolds had higher water contact angle, and the other porous scaffolds showed lower values, but the differences between the porous scaffolds and REF1 were not statistically significant. In order to investigate the influence of water contact angle on the protein adsorption ability of the porous scaffolds, Fig. 2c shows the results of the protein adsorption study. The protein adsorbed by the scaffolds after incubation for 24 hours was significantly higher than incubation for 1 hour. All the porous scaffolds had higher protein adsorption ability than REF1 ($p < 0.001$). However, no obvious regularity was observed as the porosity or pore size varied.

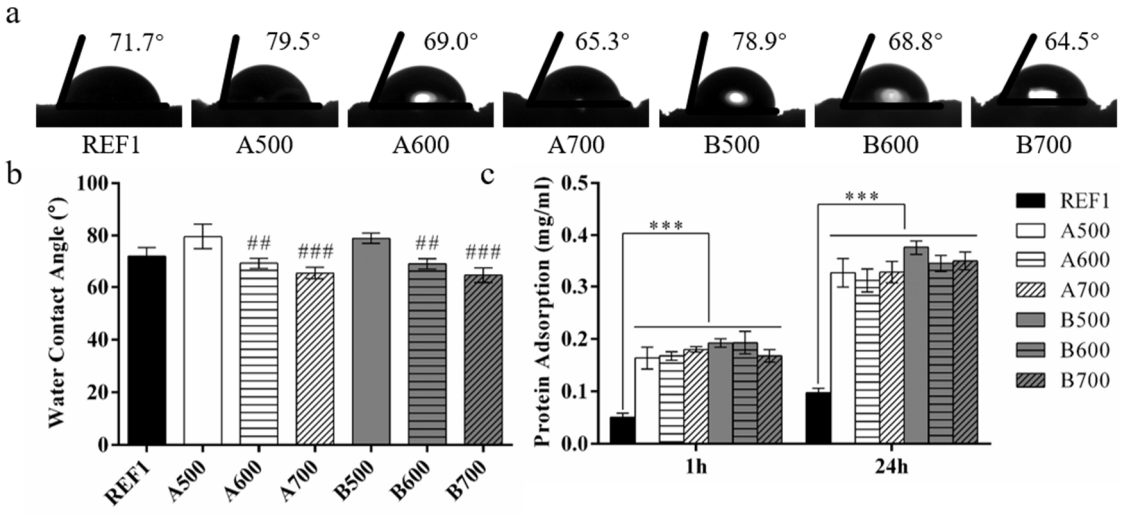

Fig. 2. Water contact angle and protein adsorption test of the SLM scaffolds. (a) image of water droplets showing measured water contact angle; (b) average water contact angle of the scaffolds; (c) adsorbed protein contents of the scaffolds. Water contact angle and adsorbed protein were analyzed by one-way ANOVA and Tukey post hoc tests. *$p < 0.05$, **$p < 0.01$ and ***$p < 0.001$ compared with REF1; #$p < 0.05$, ##$p < 0.01$ and ###$p < 0.001$ compared with A500. For each group, $n = 3$.

3.2 *In vitro* cytotoxicity and cell morphology

In order to evaluate the cytocompatibility of the scaffolds, rBMMSCs were cultured. For comparison, the

cytocompatibility of REF1 was also evaluated. CCK-8 assays were conducted to evaluate the cell viability after the cells were cultured in the 100% liquid extracts for 1, 3 and 5 days. The relative cell growth rates on the porous scaffolds and solid plate are shown in Fig. 3. Clearly, the relative growth rates were higher than 94% in all cases at different time points. However, the viability of cells cultured in 10% (v/v) DMSO was significantly lower than that of the control group.

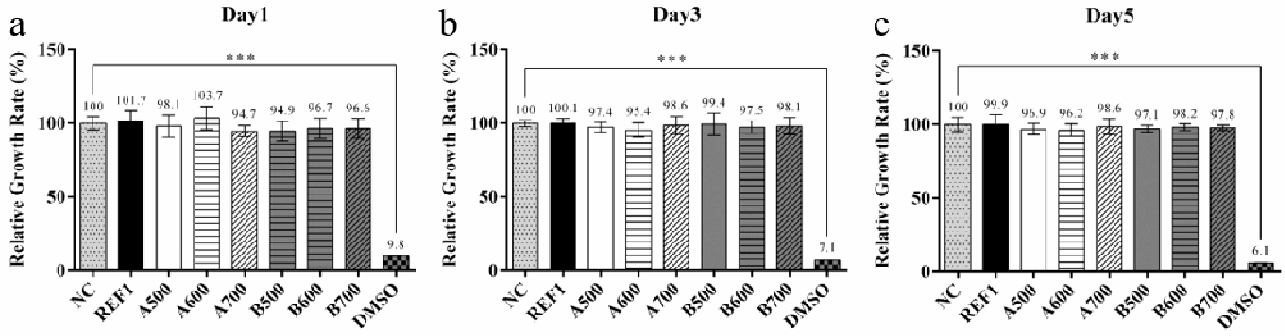

Fig. 3. Cytotoxicity test of the Ti6Al4V ELI scaffolds by CCK-8 assays. Relative growth rates were analyzed by one-way ANOVA and Tukey post hoc tests. *p < 0.05, **p < 0.01 and ***p < 0.001. For each group, n = 6.

The fluorescence images of live/dead staining of rBMMSCs seeded on the SLM porous scaffolds and REF1 were displayed in Fig. 4. In the images, the green color indicates live cells, and red color indicates dead cells. The prevalence of live cells could be seen on the scaffold surfaces with only few dead cells detected. For the porous scaffolds as shown in Fig. 4a-c (Group A) and Fig. 4 d-f (Group B), after the cells were seeded onto the scaffolds for 1 day, the cells have adhered to the struts of the scaffolds. After culture for 7 days, the number of live cells increased as shown in Fig. 4a'-c' (Group A) and Fig. 4 d'-f' (Group B). It should be noted that the cells on the struts also migrated to the back of the struts, which cannot be directly observed due to their 3D spatial characteristic. In contrast, the number of cells on the REF1 showed random distribution after culture for 1 day and 7 days (Fig. 4g and g').

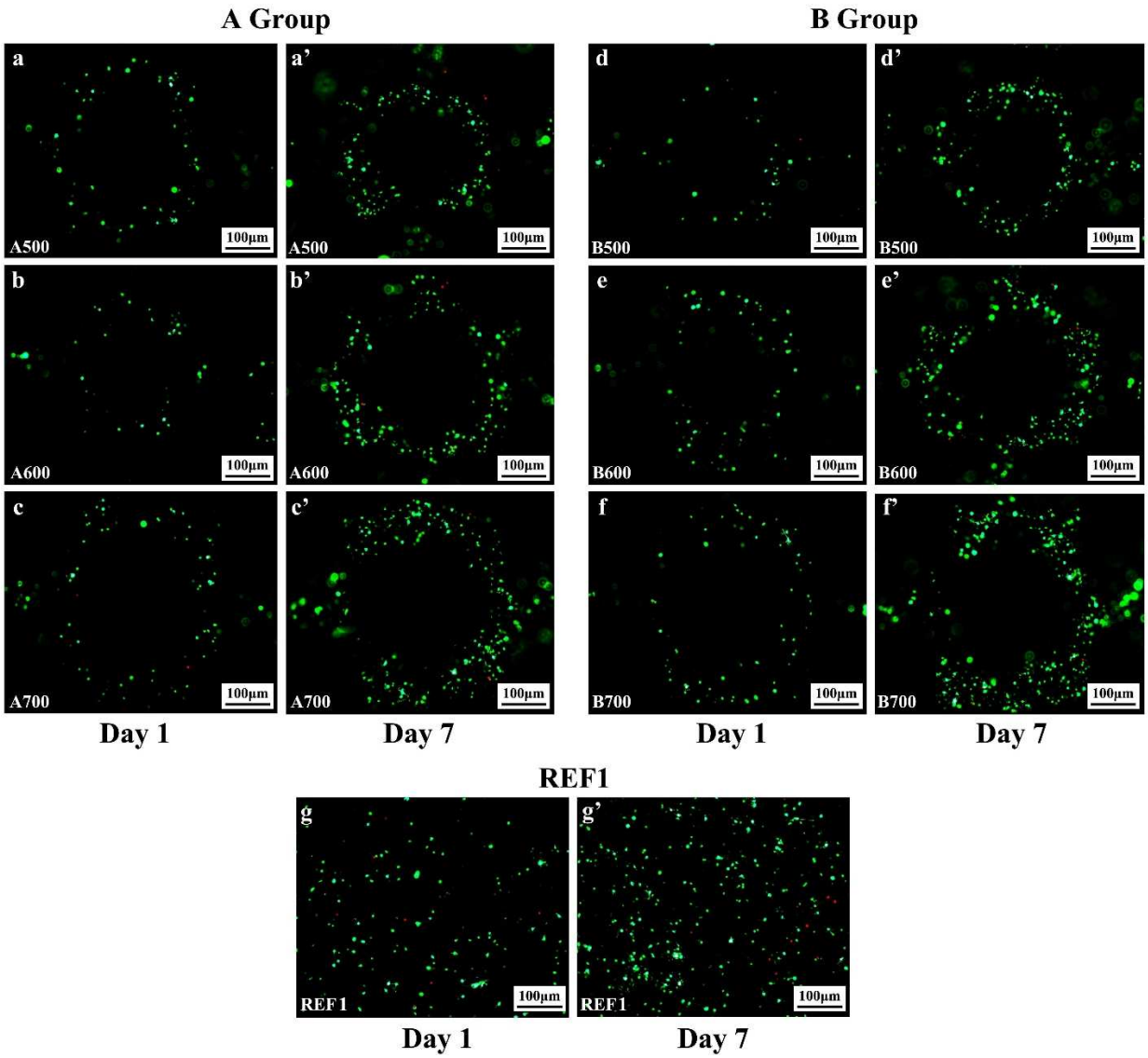

Fig. 4. Fluorescence images showing live and dead staining. Green color indicates living cells and red color indicates dead cells.

Fig. 5 shows the cell morphologies observed by SEM. Black arrows point to healthy cells which are uniformly distributed on the surface of all samples. It is seen from the low-magnification images (Fig. 5a-g) that, the adherent Ti6Al4V ELI powder particles on the struct and plate surfaces seemed to have influence on the preferential adsorption of the cells. From the high-magnification view (Fig. 5a'-g'), it is found that the cells preferentially grew within the waviness of the surfaces and particularly between small particles. This fact may indicate that larger adherent particles on the SLM Ti6Al4V ELI surface could hinder the attachment of cells.

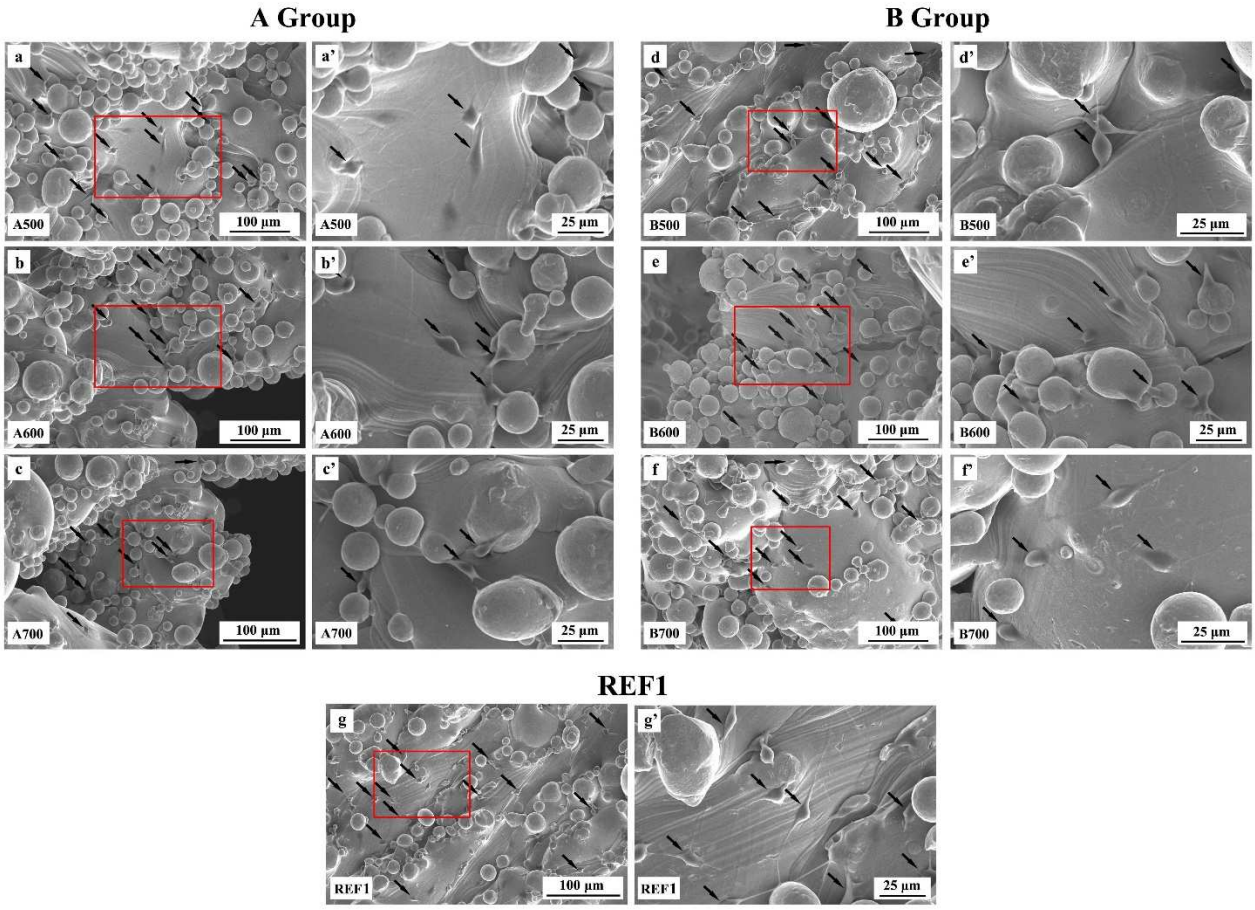

Fig. 5. SEM observation of rBMMSCs. Black arrows point to cells.

3.3 Cell proliferation

Cells expressing GFP will emit green fluorescence and can be observed using a fluorescence microscope. In order to study the effect of pores size and porosity on cell proliferation, Fig. 6 shows the fluorescent images of the cells growing on the porous scaffolds. It is seen that the number of the cells growing on the porous scaffolds increased gradually with the culture time. The difference in the fluorescent images between each scaffold became gradually significant after the cells being cultured for 3 days. After cultured for 21 days, the cells growing on the surfaces of A500 and B500 scaffolds showed the brightest green fluorescence within each group. This result suggests that cells proliferated faster on the scaffolds with a pore size of 500 μm than those with larger pore sizes. In addition, by comparing Group A (porosity of 60%) to Group B (porosity of 70%), it is seen that the cells growing on the surfaces of Group A scaffolds showed brighter green fluorescence those on the surfaces of Group B scaffolds. This fact implies that cells proliferated faster on the scaffolds with lower porosity. The fluorescent images clearly revealed that A500 scaffold was much better than the other scaffolds in facilitating cell growth.

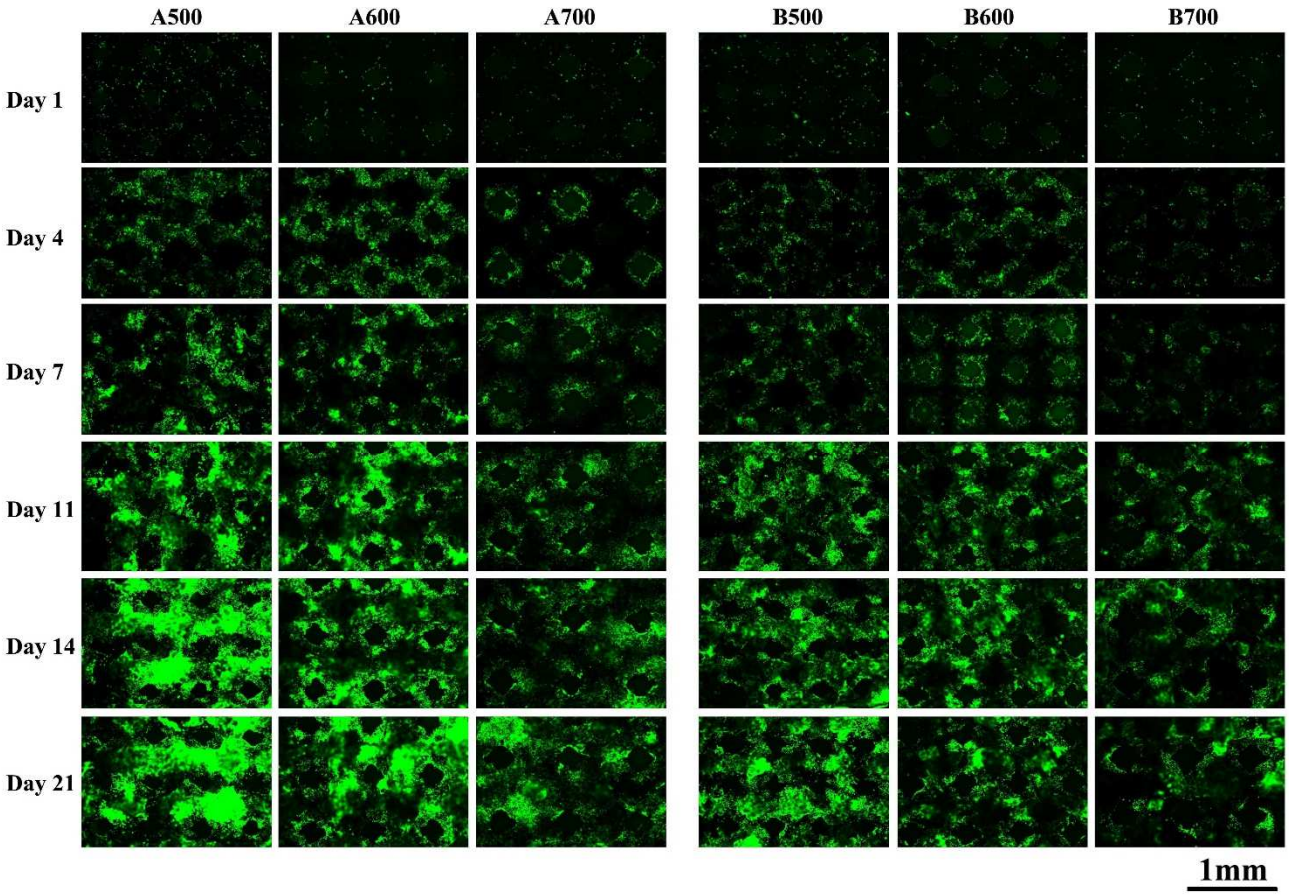

Fig. 6. Fluorescent images showing cell proliferation on the porous scaffolds.

It is known that DNA content is directly related to cell population and can help quantitatively evaluating the number of cells on the porous scaffolds. Therefore, DNA content in each scaffold was measured and the results are shown in Fig. 7. Note that the test was conducted on cell lysates which were extracted after specific time intervals. It is seen that the DNA content increased gradually with the increase in cell culture time for all the porous scaffolds. In addition, no significant difference in DNA content was observed among different porous scaffolds after culture for 1 day. However, after culture for 7 days, A500 scaffold revealed more DNA content than the other scaffolds. As the culture time further increased, the difference between A500 scaffold and the other scaffolds in DNA content became increasingly larger. DNA content study indicates that A500 scaffold is the best scaffold for cell proliferation, which is consistent with the fluorescent images shown in Fig. 6.

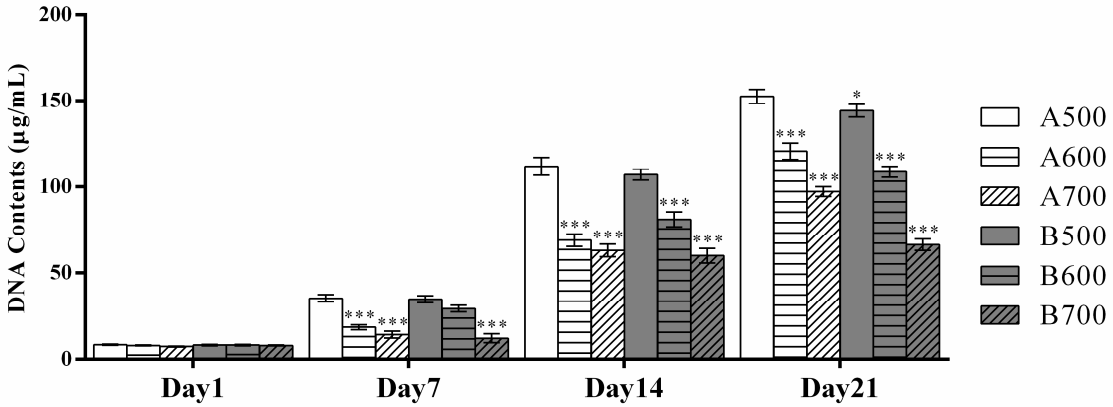

306

307 **Fig. 7**. DNA contents assessed by one-way ANOVA and Tukey post hoc tests. *p < 0.05, **p < 0.01 and ***p < 0.001 compared with
308 A500. For each group, n = 3.

309 **3.4 Osteogenic differentiation**

310 The results of osteogenic differentiation evaluation are shown in Fig. 8. For ALP activity assessment as shown in
311 Fig. 8a, after 7 days' culture, the ALP activity of cells on the porous scaffolds was lower than that on REF1. However, at
312 day 14, the ALP activity on the porous scaffolds started to exceed that on REF1. Furthermore, the ALP activity on A500
313 and B500 scaffolds was 2.52 and 1.81 times higher than on REF1 ($p < 0.001$, Fig. 8a) after culture for 21 days. The
314 results of osteogenic related gene expression were, to some extent, similar to the results of ALP activity. Briefly, the
315 expression of most osteogenic genes of cells on the porous scaffolds were lower than that on REF1 at day 7 and enhanced
316 as the culture time increased. It is worth noting that the relative expression of BMP-2 of A500 scaffold was 6 times
317 higher than that of REF1 and significantly higher than the other porous scaffolds (Fig. 8b). For COL-1, OCN and
318 RUNX-2, higher expression could also be observed on A500 scaffolds at day 21 (Fig. 8c, d, f). However, the result of
319 OPN was different (Fig. 8e). The highest expression on A500 scaffold (4.08 times) occurred on day 14 and then declined
320 to 2.28 times on day 21, and the difference between A500 scaffold and REF1 was statistically significant at these two
321 time points. More importantly, it can be seen that all tested osteogenic gene expression levels decreased from A500 to
322 A700 at day 21.

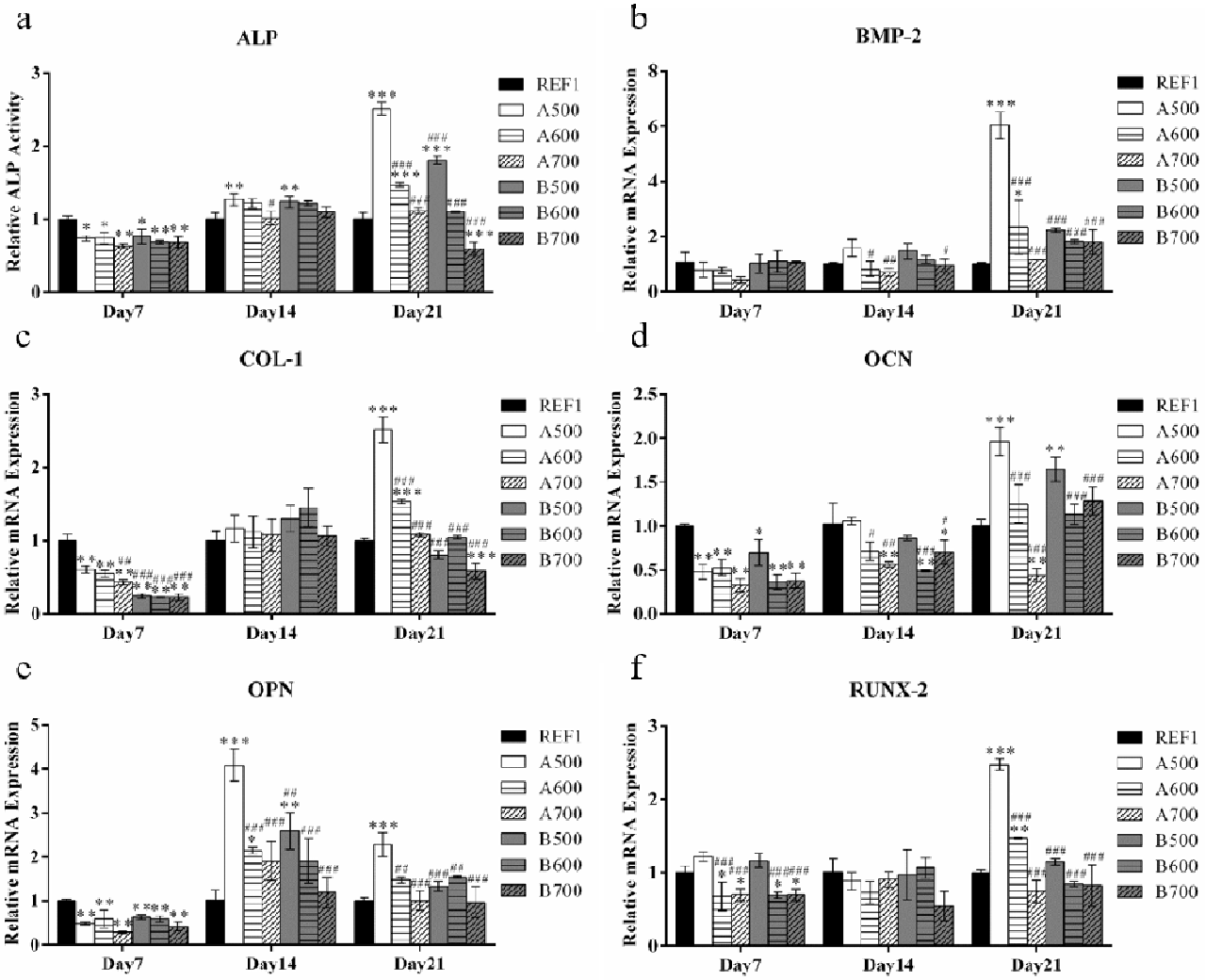

Fig. 8. Osteogenic differentiation assessed by ALP activity and express of osteogenic related genes. (a) ALP activity of the cells on different porous scaffolds; (b–f) relative mRNA expression of BMP-2, COL-1, OCN, OPN and RUNX-2 at day 7, 14 and 21. *p < 0.05, **p < 0.01 and ***p < 0.001 compared with REF1; #p < 0.05, ##p < 0.01 and ###p < 0.001 compared with A500. For each group, n = 3.

3.5 Subcutaneous implant

In order to assess the interaction between the porous scaffolds and soft tissues, *in vivo* study was conducted. The scaffolds were implanted under the back skin of the rats, and Fig. 9 shows the general results of the *in vivo* study. No obvious subcutaneous effusion, redness and infection were observed after implantation (Fig. 9a and b). As shown in Fig. 9c, d and e, after implantation for 4 weeks, soft tissues grew tightly on the surface of the scaffolds and some blood vessels could also been found.

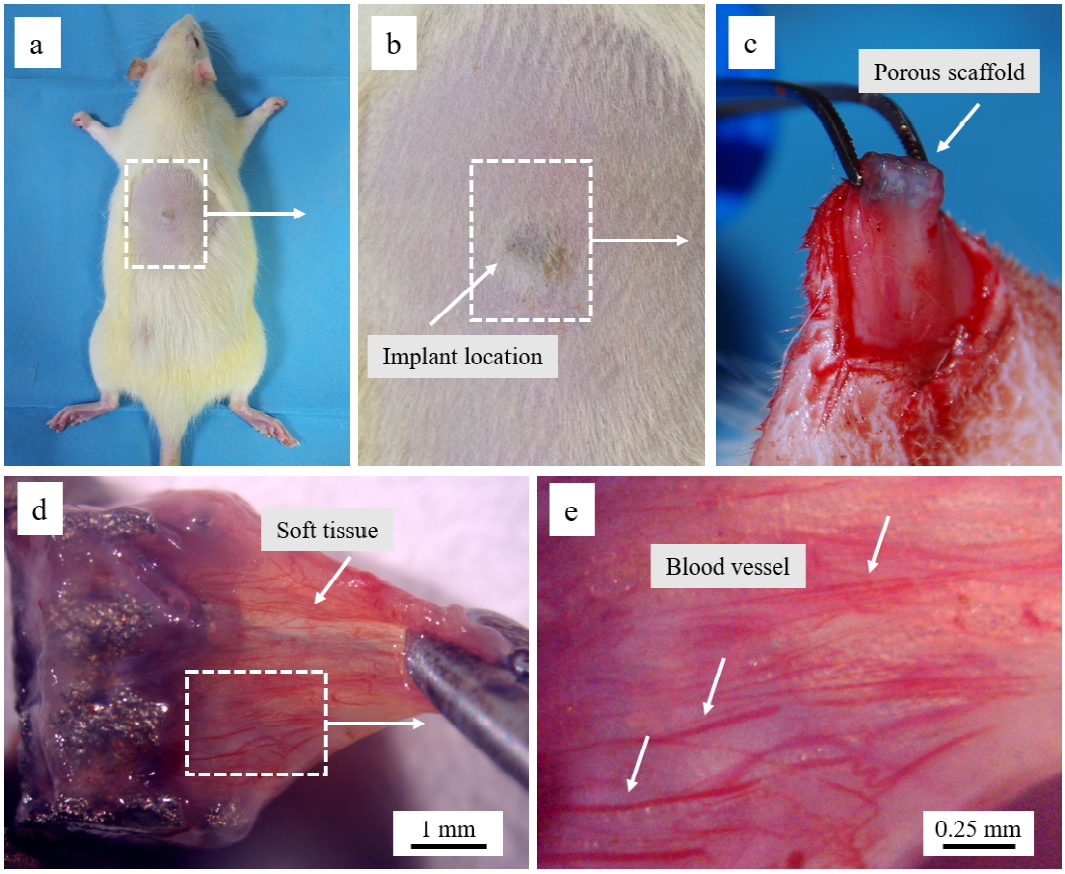

Fig. 9. General results of the *in vivo* study. (a) overview of the implant location for subcutaneous implantation; (b) magnified view of the implant location; (c) porous scaffold under the skin; (d) soft tissues on the porous scaffold; (e) magnified view of the soft tissues attached on scaffold, white arrows point to blood vessels.

3.6 Micro-CT scanning for bone ingrowth

New bone formation in the porous scaffolds was studied through μ-CT scanning. Fig. 10 shows the 3D reconstruction of the porous scaffold and surrounding bone tissues, respectively. The 3D reconstruction images of the porous implant shown in Fig. 10a provide clear evidence that new bone had grown into the porous scaffolds after healing for 12 weeks. The reconstructed spatial distribution of the new bone formation shown in Fig. 10b qualitatively illustrates the difference of bone ingrowth ability between each scaffold. As can be seen, the volume of the bone ingrowth decreased in each group as the pore size increased. Therefore, A500 and B500 scaffolds showed better new bone formation ability than the other scaffolds.

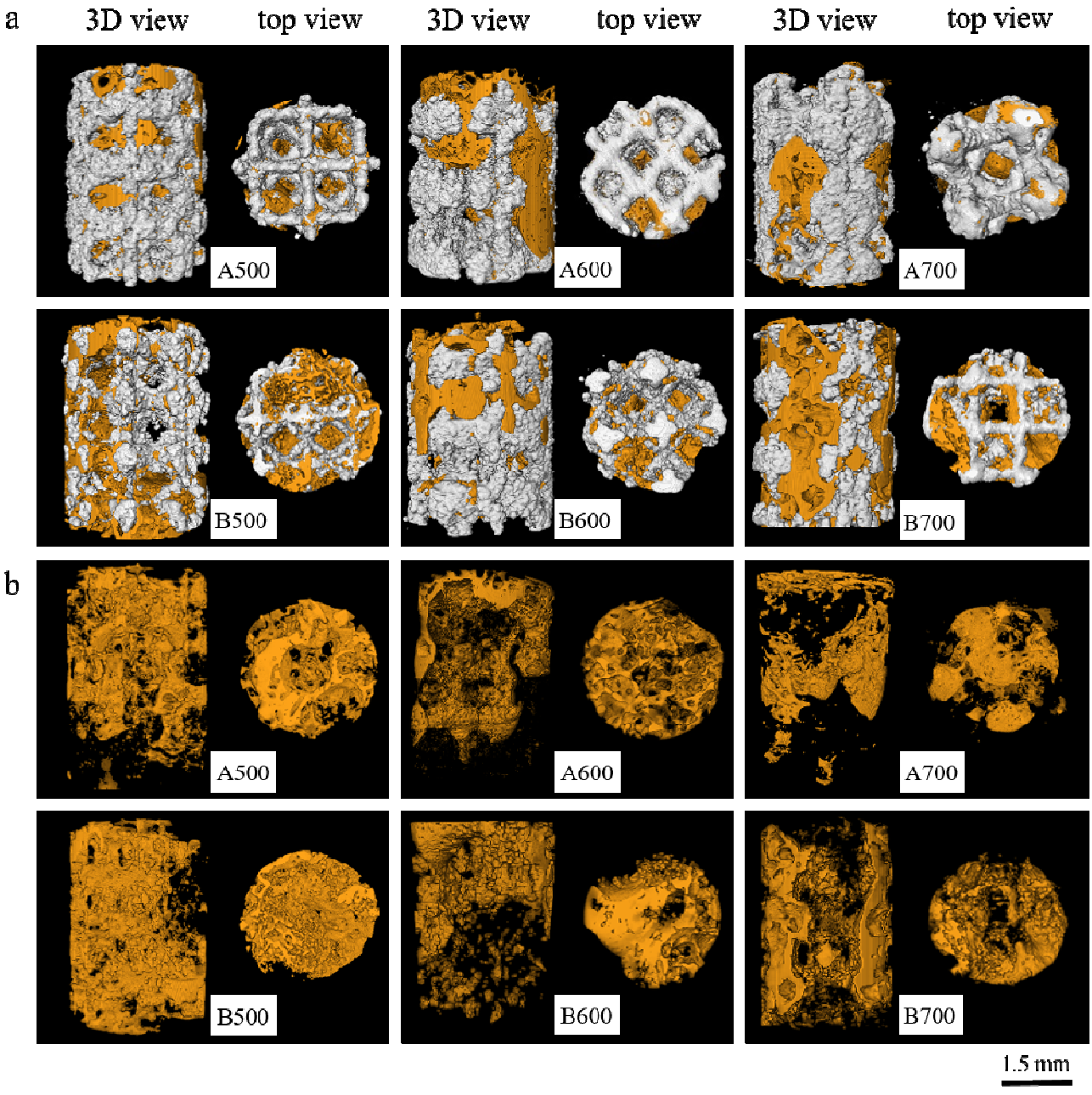

346

347 **Fig. 10**. μ-CT analysis of new bone formation. (a) reconstruction images of porous implants; (b) reconstruction images of bone
348 formation. Orange area: new bone formation.

349 The ratio of BV to TV has been widely used to quantitatively evaluate the bone ingrowth [25, 31, 32]. Therefore,
350 BV/TV was also used in this work to evaluate the effect of pore size and porosity on the bone ingrowth. Fig. 11 shows
351 the values of BV/TV of different samples (porous scaffolds and REF2) after bond healing for 12 weeks. Clearly, the
352 porous scaffolds showed better bone ingrowth than REF2, indicating the superiority of the porous scaffolds over REF2.
353 In addition, as the pore size increased, BV/TV reduced for each group, which suggests that lower pore size benefit the
354 bone growth. By comparing Group A to Group B, no obvious regularity could be found. However, among all the samples,

A500 scaffold had the highest BV/TV and hence the best bone ingrowth, which is in good agreement with the *in vitro* study.

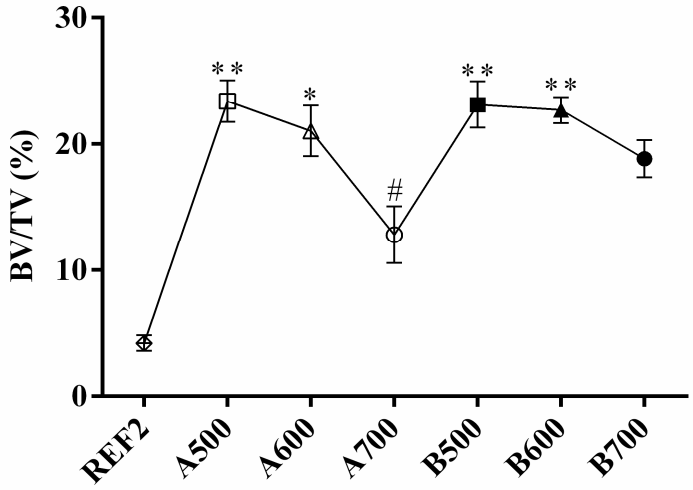

Fig. 11. The ratio of BV/TV of the porous scaffolds and reference sample (REF2). *p < 0.05, **p < 0.01 compared with REF2; #p < 0.05 with A500.

3.7 Histological evaluation

The above *in vitro* and *in vivo* studies above have shown that A500 scaffold has the best bone ingrowth. Therefore, the osteointegration of the bone and A500 scaffold was further assessed by Van-Gieson staining. The results after implantation for 4 weeks and 12 weeks were showed in Fig. 12. Note that the red area represents new bone tissues and blue area represents fibrous tissues. As can be seen, after implantation for 4 weeks, newly generated bone started to grow into the pore space of A500 scaffold from the surrounding bone tissues. In addition, it is also found that the bone tissues adhered tightly to the surfaces of the scaffold, which indicates a good osteointegration. In addition, the newly regenerated bone tissues increased as healing progressed. After implantation for 12 weeks, it is obvious that new bone can be detected in the central area of the scaffold, which is consistent with the results of μ-CT.

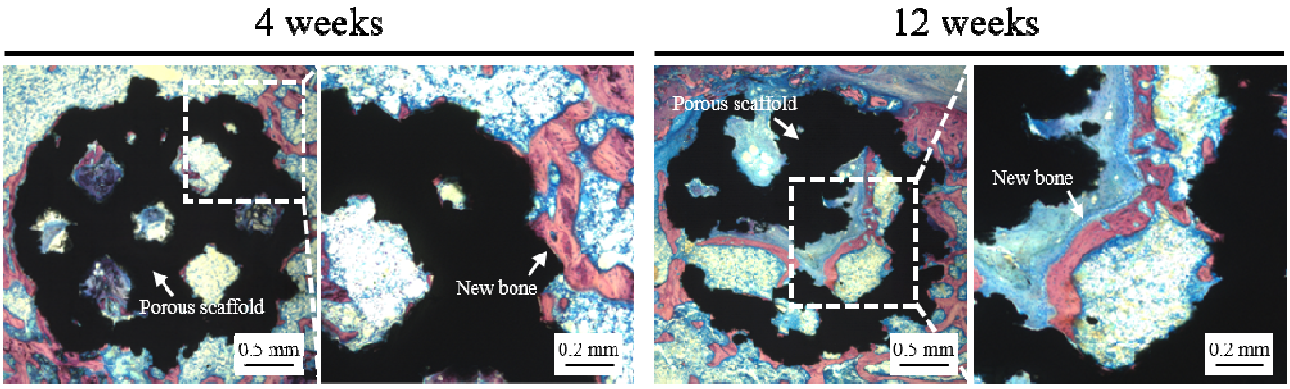

Fig. 12. Histological assessment of A500 scaffold by VG staining after implantation for 4 and 12 weeks. The scaffold implant is black, new bone is stained red, fibrous tissues is stained blue.

4 Discussion

Large bone defect is still a challenge for orthopedists, as even the "gold standard" treatment, autologous bone graft, would face some drawbacks [33, 34]. In the past few years, Ti and its alloys have been widely studied for orthopedic applications [35-37]. The results of these studies reveal the promising prospects of Ti alloys. Porous Ti and Ti alloys have many advantages over traditional solid metal materials. Porous scaffolds significantly reduce stress shielding effects and prevent mechanical failure. Furthermore, the interconnected pore structure is proven to be beneficial to vascularization, nutrient-waste exchange, osteoconduction and bone ingrowth, which leads to good osseointegration and long-term stability [13]. In this study, SLM technology was used to manufacture porous Ti6Al4V ELI scaffolds with pore sizes of 500, 600 and 700 μm and porosities of 60% and 70%. The microstructure evolution and mechanical performance of these SLM porous scaffolds have already been investigated and published elsewhere [18, 38]. The results have suggested that the porous Ti6Al4V ELI scaffolds had sufficiently high mechanical strength and comparable elastic module to the real bone, which is the fundamental of the current research. Further to the mechanical properties, in this study, the biomedical properties of these scaffolds were systematically investigated through well-designed *in vitro* and *in vivo* experiments. Special attention was paid on the determination of optimum scaffold porosity and pore size for bone substitute.

The SLM porous scaffolds with different surface roughness can lead to different wettability and thus influence the permeability of the scaffolds. The contact angles of all the scaffolds were smaller than 80°, indicating a hydrophobic surface. The values of the contact angles of A500 and B500 scaffolds were higher than those of REF1, which could contribute to the side effect on the water drop molding into the scaffolds [25]. In each group, with the increase of pore size or porosity, the contact angle gradually decreased (see Fig. 2b). It can be speculated that the porous scaffolds with higher porosity show more hydrophilic surfaces due to their relatively higher surface roughness [39]. Cytoactivity of the

cells on the material surface could be greatly affected by the adsorption ability of proteins, which was beneficial to cell accommodation and proliferation [40]. Moreover, the adsorption capacity of proteins was directly related to surface wettability, which was greatly influenced by the surface roughness. Consequently, the cell viability on the tested samples could be attributed to the different scaffold surface properties caused by different porosities and pore sizes. Although the ratio of surface to volume (BS/TV) of each scaffold were different, the difference in proteins that were adsorbed by the scaffolds was not statistically significant after culture for 1 hour. As the soaking time increased to 24 hours, the scaffolds with higher porosity displayed slightly higher protein adsorption, which is similar to the result of a previous study [41]. Furthermore, all the scaffolds showed obvious higher protein adsorption ability than REF1 at the prescribed time of 1 hour and 24 hours ($p < 0.001$) (see Fig. 2c), because BS/TV of porous scaffolds are much higher than that of Ti6Al4V plate. Proper wettability and protein adsorptive ability of the porous scaffolds could provide a suitable environment for cell adhesion and proliferation.

The cytocompatibility of the porous scaffolds was qualitatively assessed by CCK-8 assay, live/dead staining, and SEM observation. According to ISO 10993, for a biocompatible material, the viability of cells cultured in its 100% liquid extracts should not fall below 70% compared to a blank and negative (nontoxic) control. In this assessment, the viability of the cells in 100% liquid extracts of all the porous scaffolds was above 90% compared to the negative control after being cultured for 1, 3 and 5 days (see Fig. 3). Live/dead staining showed that there were few dead cells on the scaffolds after the rBMMSCs were seeded directly onto the scaffolds. Then, after culture for 7 days, the green fluorescence (live cells) increased, while the red fluorescence (dead cells) remained at a low level, which indicates that cells proliferated normally on the surface of the scaffolds. From the SEM images, the cells on the porous scaffolds exhibited a well-spread shape and drifted to the inner space of the interconnected porous scaffolds, which can promote nutrient-waste exchange and hence benefit to cell culture. In previous reports [42, 43], it was found that a porous structure with a high surface area and average curvature conduce to induce tissue amplification *in vitro*. Moreover, the rough surface could increase the anchorage possibility of bone cells in addition to the surface energy of the materials, which benefited the adsorption of macromolecules and the attachment of cells. Furthermore, the rough interface had a similar curvature to bone cells, which helped the physical/chemical combination of the cells or macromolecules [3, 44]. However, it is found that the cells preferentially grew within the waviness of the surfaces and particularly between small particles. Larger powder particles adhered to the strut surfaces could hinder the attachment of cells and may bring risks to human health due to the high possibility of flaking from the strut surface after implantation. The findings in this work clearly showed the good cytocompatibility of the porous Ti6Al4V ELI scaffolds.

The proliferation of the cells on the scaffolds using rBMMSCs expressing GFP were investigated, which can emit green fluorescence, due to the good adhesion environment provided by the scaffolds. The fluorescent images of the cells on the scaffolds were captured at different time points during 21-day culture period (Fig. 6). It is worth noting that after the same amounts of cells were seeded, more cells could be observed in A500 and B500 scaffolds than in the other porous scaffolds within each group after culture for 7 days. In the designed model, as can be seen in Fig. 2, the shape of the struts is rectangle, while after the laser processing the rectangle struts could be transformed into approximately cylindrical struts. As the culture time increased, significant difference in the cell proliferation was gradually observed. Rumpler et al. [45] quantitatively studied the growth kinetics of collagenous tissues in an osteoblast culture for different 3D channel geometries. They concluded that the mechanism of curvature-driven tissue growth, that is, the amount of tissues deposited in the geometries was proportional to the local curvature. This means that the local curvature of the scaffolds could affect the tissue formation kinetics, which could further influence the cell deposition result. Having the highest curvature, A500 scaffold exhibited the brightest green fluorescence (Fig. 6), which could be explained by this curvature-driven mechanism [45].

In previous research, Chang et al. [25] investigated the influence of the pore size of porous Ti on cell penetration and bone ingrowth. The results illustrated that the porous scaffolds with a pore size of 188 μm were covered by cells; however, the oxygen and nutrient exchange were affected, which led to cell death inside the scaffold. Furthermore, Xue et al. [42] suggested that an optimum pore size of larger than 200 μm could be favorable to cell ingrowth into the pore structures. Knychala et al. [46] qualitatively studied the forces exerted by cells which could drive proliferation and increase with curvature. They also assumed that as the curvature increased, the net force exerted on the underlying tissues would increase. Moreover, to investigate the influence of pore size, Hollander et al. [47] cultured human osteoblasts on porous Ti6Al4V ELI discs with the nominal pore diameters of 500, 700 and 1000 μm. The specimens of 500 μm showed predominant overgrown with cells, which is similar to our results. In our study, although the pores of the porous scaffolds were not completely covered by cells, a predominant trend of cells attached on A500 scaffold after seeding for 21 days could be observed. This means that the transport of nutrients and the emission of metabolites could be ensured by A500 scaffold. The DNA content assay confirms this observation and suggests that A500 scaffold was more appropriate for cell penetration and proliferation than the other scaffolds. This could be explained by the following two aspects. First, the scaffolds with a small pore size of 500 μm had higher seeding efficiency. It was reported that porous scaffolds with a lower pore size may lead to inferior permeability [48, 49], which could result in lower fluid velocity and higher cell seeding efficiency [25]. Higher permeability led to higher fluid velocities, allowing cells to attach on the surface of the

scaffold with less time. The contact angle measurements supported this fact. Second, A500 scaffold had the largest surface area, which could provide larger surface area for cell adsorption and proliferation. For the scaffolds with the same pore size, the number of cells on the scaffolds with a porosity of 60% was higher than those with a porosity of 70%, which suggests that the porosity of 60% was better for vascularization and more beneficial to nutrient and oxygen exchange and cell penetration [50].

The expression of ALP and COL-1 during the formation and maturation of extracellular bone matrix, and the expression of OCN and OPN during the process of bone matrix mineralization, are main indications of osteogenic differentiation. All the cells on the scaffolds were supplemented with osteogenic medium to evaluate the influence of pore size and porosity on osteogenic differentiation. At day 7, RT-PCR profiling exhibited relatively lower expression of osteogenic genes (BMP-2, OCN, OPN and RUNX-2) for the porous scaffolds than for REF1. Previous studies suggested that the excessive space of porous scaffolds may delay the differentiation process in the initial stage [25, 51]. ALP and COL-1 are markers of osteoblast differentiation and maturation which can promote cell differentiation and reflect the phenotypic characteristics of osteogenic differentiation, respectively. At day 14, no significant differences in ALP and COL-1 could be found. Moreover, higher expression of ALP and COL-1 for A500 scaffold could be seen at day 21, indicating that the cells on A500 scaffold had better differentiation performance. BMP-2 and OPN facilitate the development of bone and cartilage and are beneficial to the mineralization of bone, respectively. The expression of the osteogenic genes (BMP-2 and OPN) for the porous scaffolds was higher than that for REF1 at day 14. Specifically, the expression of OPN for A500 scaffold was 4 times higher than that for REF1 (Fig. 8). At day 21, all the osteogenic genes for A500 were significantly higher than REF1 (6 times for BMP-2, 2.5 times for COL-1, 1.7 times for OCN, 2.2 times for OPN, 2.5 times for RUNX-2). It should be noted that the osteogenic gene for A500 scaffold was also significantly higher than that for the other porous scaffolds. These results may be explained by the mechano-transduction mechanism, which is a hypothesis with regard to stimuli and cell differentiation [25, 52]. It is suggested that cells on implants with relatively small pores were more inclined to differentiate as they had more chance to feel stimuli from different struts [53-55]. In this study, A500 had more struts within the same volume, which was beneficial to cell differentiation. Furthermore, based on the results of cell proliferation, the number of cells on A500 was greater than on the other scaffolds. This could be due to the direct cell-cell contacts which significantly enhanced the osteogenic differentiation of rBMMSCs owing to the rapid transduction of cell signaling molecules through their gap junctions [56].

Evident adhesion of soft tissues on the porous scaffolds could be observed after subcutaneous implantation for 4 weeks (Fig. 9), which shows good biocompatibility and ability for tissues ingrowth [40]. Moreover, the formation of

blood vessels is a favorable sign for tissue penetration, since productive exchange of oxygen and nutrients are beneficial to bone regeneration.

μ-CT scanning can evaluate bone formation qualitatively through radiography and quantitatively through 3D ingrowth in a non-destructive way. Different bone ingrowth can be observed in the reconstruction images after 12 weeks of healing (Fig. 10). Bone ingrowth towards the interior of the porous scaffolds can be seen, which led to the density of the bone decreasing gradually from outside to inside. Moreover, bone ingrowth could be found in all locations of the porous scaffolds. The detailed results of bone ingrowth are displayed in Fig. 11. As can be seen, in each group, the porous scaffolds with 500 μm pore size showed the highest BV/TV ratios, which were 23.41% for A500 scaffold and 23.15% for B500 scaffold. For the scaffolds in group A, the BV/TV ratio decreased to 21.04% when the pore size increased from 500 μm to 600 μm, and further decreased to 12.81% when the pore size increased to 700 μm. The same trend can also be observed in group B. It has been reported that when a scaffold was implanted into a host, cell adhesion was the first cellular event, which greatly affected subsequent cellular biological functions, including proliferation, differentiation, and tissues formation [57-59]. The results of the *in vivo* study in this work are consistent with the conclusions of *in vitro* studies where A500 and B500 scaffolds provided a better condition for cell penetration and differentiation than the other scaffolds. Moreover, the BV/TV ratio of all the porous scaffolds were significantly higher than that of REF2 (4.27%), and no new bone formation could be detected in the middle of the defects of REF2. The histological staining results also confirm that newly generated bone tissues were found in the pore space of the scaffolds and good integration of bone tissues and scaffolds were achieved. These results clearly indicate that the porous scaffolds are suitable for cell penetration and bone ingrowth into the center of the bone defects and accelerates the restoration of bone defects. Based on the results obtained in this work, A500 scaffold with the lowest pore size and porosity had the most promising cell penetration and bone ingrowth. Therefore, A500 is suggested the optimum scaffold for bone implant. While, it should be noticed that the optimum pore size and porosity identified in this paper is only applicable to octahedral cell structure but not a universal conclusion.

SLM products typically have complex structures (e.g., lattice structures produced in this work), and hence it is very difficult to quantify the geometrical comparability between the CAD design and as-built structure using traditional metrology techniques [60, 61]. Due to the staircase and balling effect, powder adhesion is an inevitable phenomenon in the SLM fabricating process [62, 63]. The adhered powders on the sample surface have high risks of detaching from the base structure and will be harmful to human bodies, which have to be removed before implantation. In some studies, traditional grinding or sandblasting method have been adapted to remove the residual powders on the sample surface [64,

65]. However, it is difficult to process samples with complex internal structures through the traditional surface treatment methods. Dual acid etching process is the most popular chemical method [66] to polish SLM porous structures. Wysocki et.al. [67, 68] proved that chemical polishing with hydrofluoric (HF) acid or HF acid + nitric acid (HNO_3) is an effective way for the removal of partially molten powder particles on the porous scaffolds as the acid-based solutions can penetrate into the porous structures through the interconnected pores. The pore sizes after HF/HNO_3 treatment were almost equal to those designed in the CAD models. The HF/HNO_3 treated structures even showed a decrease in water contact angle and had no negative effect on neither cell proliferation and differentiation, which demonstrates the potentials of chemical polishing method for removing the partially molten powder particles. Although the current work did not include the surface post-treatment procedure, considering its importance, it is encouraged that future *in-vitro* or *in-vivo* studies shall take the HF/HNO_3 surface treatment into account before any biological tests.

Compared to autologous bone graft and other synthetic bone graft substitutes, the SLM porous Ti6Al4V ELI scaffolds produced in this work provide better biocompatibility and long-term stability due to their superior bone ingrowth. Therefore, they are conducive to fulfilling biological fixation. Lower stress shielding led to earlier defect bridging, increased bone formation, and advanced bony regeneration of the critical size defect.

Conclusions

This paper conducts a systematic investigation on the SLM porous Ti6Al4V ELI scaffolds for bone implantation based on well-designed *in vitro* and *in vivo* experiments. Scaffolds with pore sizes of 500 μm, 600 μm and 700 μm and porosities of 60% and 70% were studied and compared with each other. The *in vitro* experimental results indicate that cell proliferation and differentiation were significantly dependent on the pore size and porosity of the porous scaffolds. On the basis of the porous scaffolds used in this work, it is found that lower pore size and porosity resulted in better cell adhesion, proliferation and osteogenic differentiation of rBMMSCs. Particularly, the scaffold with a pore size of 500 μm and porosity of 60% showed the best results. In the *in vivo* study, the μ-CT analysis revealed that the scaffold with a pore size of 500 μm and porosity of 60% also had the highest BV/TV value and hence the best bone ingrowth among all the scaffolds. Therefore, based on the findings in this work, it is plausible to suggest that the SLM porous Ti6Al4V ELI scaffold with a pore size of 500 μm and porosity of 60% is a promising for the fabrication of porous load-bearing implants for cementless fixation (e.g., acetabular cup and hip prosthesis).

Acknowledgements

The authors would like to acknowledge financial supports provided by the founds of Guangdong Academy of

Science Projects 2019GDASYL-0502006, Science and Technology Planning Project of Guangdong province (2016B090916003), Science and Technology Planning Project of Guangzhou (201704030111), 201807010030, 2017A070701027, 2016A030312015, 2017G1FC0008, 2018GDASCX-0402. Sanming Project of Medicine in Shenzhen （SZSM201612023）

Conflicts of interest statement

The authors report no conflicts of interest in this work.

References

[1] D.A. Belatti, A.J. Pugely, P. Phisitkul, A. Amendola, J.J. Callaghan, The Journal of Arthroplasty, 29 (2014) 1539-1544.
[2] N. Taniguchi, S. Fujibayashi, M. Takemoto, K. Sasaki, B. Otsuki, T. Nakamura, T. Matsushita, T. Kokubo, S. Matsuda, Materials science & engineering. C, Materials for biological applications, 59 (2016) 690-701.
[3] M. Fousova, D. Vojtech, J. Kubasek, E. Jablonska, J. Fojt, J Mech Behav Biomed Mater, 69 (2017) 368-376.
[4] B. Dutta, F.H. Froes, Metal Powder Report, 72 (2017) 96-106.
[5] L.H.M. Antunes, C.R.P. de Lima, Cobalt-Chromium Alloys – Properties and Applications☆, Reference Module in Materials Science and Materials Engineering, Elsevier, 2017.
[6] A. Goharian, M. Abdullah, Trauma Plating System. Amsterdam: Elsevier, (2017) 115-142.
[7] P.K. Zysset, X.E. Guo, C.E. Hoffler, K.E. Moore, S.A. Goldstein, Journal of biomechanics, 32 (1999) 1005-1012.
[8] D.K. Pattanayak, A. Fukuda, T. Matsushita, M. Takemoto, S. Fujibayashi, K. Sasaki, N. Nishida, T. Nakamura, T. Kokubo, Acta Biomater, 7 (2011) 1398-1406.
[9] Y. Kosashvili, D. Backstein, O. Safir, D. Lakstein, A.E. Gross, The Journal of Bone and Joint Surgery. British volume, 91-B (2009) 870-876.
[10] P. Derome, A. Sternheim, D. Backstein, M. Malo, The Journal of Arthroplasty, 29 (2014) 122-126.
[11] Y. Li, C. Yang, H. Zhao, S. Qu, X. Li, Y. Li, Materials (Basel), 7 (2014) 1709-1800.
[12] R. Wauthle, J. van der Stok, S. Amin Yavari, J. Van Humbeeck, J.P. Kruth, A.A. Zadpoor, H. Weinans, M. Mulier, J. Schrooten, Acta Biomater, 14 (2015) 217-225.
[13] G. Li, L. Wang, W. Pan, F. Yang, W. Jiang, X. Wu, X. Kong, K. Dai, Y. Hao, Scientific reports, 6 (2016) 34072.
[14] B. Vandenbroucke, J.P. Kruth, Rapid Prototyping Journal, 13 (2007) 196-203.
[15] X. Yan, C. Huang, C. Chen, R. Bolot, L. Dembinski, R. Huang, W. Ma, H. Liao, M. Liu, Surface and Coatings Technology, 371 (2019) 161-171.
[16] B. Vandenbroucke, J.-P. Kruth, RAPID PROTOTYPING J, 13 (2007) 196-203.
[17] L. Thijs, F. Verhaeghe, T. Craeghs, J.V. Humbeeck, J.-P. Kruth, Acta Materialia, 58 (2010) 3303-3312.
[18] X. Yan, S. Yin, C. Chen, C. Huang, R. Bolot, R. Lupoi, M. Kuang, W. Ma, C. Coddet, H. Liao, M. Liu, Journal of Alloys and Compounds, 764 (2018) 1056-1071.
[19] A. Fukuda, M. Takemoto, T. Saito, S. Fujibayashi, M. Neo, D.K. Pattanayak, T. Matsushita, K. Sasaki, N. Nishida, T. Kokubo, T. Nakamura, Acta Biomater, 7 (2011) 2327-2336.
[20] B. Wysocki, J. Idaszek, J. Zdunek, K. Rożniatowski, M. Pisarek, A. Yamamoto, W. Święszkowski, International journal of molecular sciences, 19 (2018) 1619.
[21] L. Rony, R. Lancigu, L. Hubert, Morphologie, 102 (2018) 231-242.
[22] Z.J. Wally, A.M. Haque, A. Feteira, F. Claeyssens, R. Goodall, G.C. Reilly, J Mech Behav Biomed Mater, 90 (2019)

20-29.
[23] J. Wieding, T. Lindner, P. Bergschmidt, R. Bader, Biomaterials, 46 (2015) 35-47.
[24] F. Li, J. Li, G. Xu, G. Liu, H. Kou, L. Zhou, Journal of the Mechanical Behavior of Biomedical Materials, 46 (2015) 104-114.
[25] B. Chang, W. Song, T. Han, J. Yan, F. Li, L. Zhao, H. Kou, Y. Zhang, Acta Biomater, 33 (2016) 311-321.
[26] M. Kruyt, J.D. de Bruijn, C. Wilson, F. Oner, C. Van Blitterswijk, A. Verbout, W. Dhert, Tissue engineering, 9 (2003) 327-336.
[27] S. Yin, X. Yan, C. Chen, R. Jenkins, M. Liu, R. Lupoi, Journal of Materials Processing Technology, 255 (2018) 650-655.
[28] X. Yan, C. Chen, C. Huang, R. Bolot, M. Kuang, W. Ma, C. Coddet, H. Liao, M. Liu, Journal of Alloys and Compounds.
[29] T.B. Kim, S. Yue, Z. Zhang, E. Jones, J.R. Jones, P.D. Lee, Journal of Materials Processing Technology, 214 (2014) 2706-2715.
[30] L. Zhao, L. Liu, Z. Wu, Y. Zhang, P. Chu, Biomaterials, 33 (2012) 2629-2641.
[31] D. Agius, K.I. Kourousis, C. Wallbrink, T. Song, Materials Science and Engineering: A, 701 (2017) 85-100.
[32] K. Kapat, P.K. Srivas, A.P. Rameshbabu, P.P. Maity, S. Jana, J. Dutta, P. Majumdar, D. Chakrabarti, S. Dhara, ACS applied materials & interfaces, 9 (2017) 39235-39248.
[33] S. Green, Clin. Orthop. Relat. Res., (1994) 111-117.
[34] R. Capanna, D.A. Campanacci, N. Belot, G. Beltrami, M. Manfrini, M. Innocenti, M. Ceruso, Orthopedic Clinics of North America, 38 (2007) 51-60.
[35] A.-M. Pobloth, S. Checa, H. Razi, A. Petersen, J.C. Weaver, K. Schmidt-Bleek, M. Windolf, A.Á. Tatai, C.P. Roth, K.-D. Schaser, G.N. Duda, P. Schwabe, Science Translational Medicine, 10 (2018) eaam8828.
[36] R. Yan, D. Luo, H. Huang, R. Li, N. Yu, C. Liu, M. Hu, Q. Rong, Sci Rep, 8 (2018) 750.
[37] B. Yin, B. Xue, Z. Wu, J. Ma, K. Wang, Am J Transl Res, 10 (2018) 474-482.
[38] X. Yan, Q. Li, S. Yin, Z. Chen, R. Jenkins, C. Chen, J. Wang, W. Ma, R. Bolot, R. Lupoi, Z. Ren, H. Liao, M. Liu, Journal of Alloys and Compounds, 782 (2019) 209-223.
[39] R.N. Wenzel, Industrial & Engineering Chemistry, 28 (1936) 988-994.
[40] K. Kapat, P.K. Srivas, A.P. Rameshbabu, P.P. Maity, S. Jana, J. Dutta, P. Majumdar, D. Chakrabarti, S. Dhara, ACS applied materials & interfaces, 9 (2017) 39235-39248.
[41] F. Fang, J. Satulovsky, I. Szleifer, Biophysical journal, 89 (2005) 1516-1533.
[42] W. Xue, B.V. Krishna, A. Bandyopadhyay, S. Bose, Acta Biomater, 3 (2007) 1007-1018.
[43] R. Stangl, B. Rinne, S. Kastl, C. Hendrich, European Cells and Material, 2 (2001) 1-9.
[44] P. Heinl, L. Muller, C. Korner, R.F. Singer, F.A. Muller, Acta Biomater, 4 (2008) 1536-1544.
[45] M. Rumpler, A. Woesz, J.W. Dunlop, J.T. van Dongen, P. Fratzl, Journal of the Royal Society, Interface, 5 (2008) 1173-1180.
[46] J. Knychala, N. Bouropoulos, C.J. Catt, O.L. Katsamenis, C.P. Please, B.G. Sengers, Annals of biomedical engineering, 41 (2013) 917-930.
[47] D.A. Hollander, M. von Walter, T. Wirtz, R. Sellei, B. Schmidt-Rohlfing, O. Paar, H.J. Erli, Biomaterials, 27 (2006) 955-963.
[48] S. Impens, Y. Chen, S. Mullens, F. Luyten, J. Schrooten, Tissue Eng Part C Methods, 16 (2010) 1575-1583.
[49] S. Van Bael, Y. Chai, S. Truscello, M. Moesen, G. Kerckhofs, H. Van Oosterwyck, J. Kruth, J. Schrooten, Acta Biomater, 8 (2012) 2824-2834.
[50] V. Karageorgiou, D. Kaplan, Biomaterials, 26 (2005) 5474-5491.
[51] J. Yan, C. Zhang, Y. Zhao, C. Cao, K. Wu, L. Zhao, Y. Zhang, Biomaterials, 35 (2014) 7734-7749.

[52] A. Ataee, Y. Li, M. Brandt, C. Wen, Acta Materialia, 158 (2018) 354-368.
[53] G. Stein, J. Lian, T. Owen, FASEB J., 4 (1990) 3111-3123.
[54] E. Tsuruga, H. Takita, H. Itoh, Y. Wakisaka, Y. Kuboki, J. Biochem., 121 (1997) 317-324.
[55] G. Reilly, A. Engler, J Biomech, 43 (2010) 55-62.
[56] P.-Y. Wang, D.T. Bennetsen, M. Foss, T. Ameringer, H. Thissen, P. Kingshott, ACS applied materials & interfaces, 7 (2015) 4979-4989.
[57] L. Bacakova, E. Filova, M. Parizek, T. Ruml, V. Svorcik, Biotechnol. Adv., 29 (2011) 739-767.
[58] Y. Estrin, E. Ivanova, A. Michalska, V. Truong, R. Lapovok, R. Boyd, Acta Biomater, 7 (2011) 900-906.
[59] Y.R. Yun, J.E. Won, E. Jeon, S. Lee, W. Kang, H. Jo, J.H. Jang, U.S. Shin, H.W. Kim, Journal of tissue engineering, 2010 (2010) 218142.
[60] A. Hadi, F. Vignat, F. Villeneuve, 2015.
[61] M. Suard, P. Lhuissier, R. Dendievel, J.-J. Blandin, F. Vignat, F. Villeneuve, Powder Metallurgy, 57 (2014) 190-195.
[62] C. Yan, L. Hao, A. Hussein, P. Young, D. Raymont, Materials & Design, 55 (2014) 533-541.
[63] G. Thomann, C. Magnier, F. Villeneuve, R. Palluel-Germain, Disability and Rehabilitation: Assistive Technology, 11 (2016) 695-700.
[64] W. Peng, L. Xu, J. You, L. Fang, Q. Zhang, Biomedical engineering online, 15 (2016) 85.
[65] J.R. Strub, E.D. Rekow, S. Witkowski, The Journal of the American Dental Association, 137 (2006) 1289-1296.
[66] P.R. Klokkevold, P. Johnson, S. Dadgostari, J.E. Davies, A. Caputo, R.D. Nishimura, Clinical oral implants research, 12 (2001) 350-357.
[67] B. Wysocki, J. Idaszek, K. Szlazak, K. Strzelczyk, T. Brynk, K.J. Kurzydlowski, W. Swieszkowski, Materials (Basel), 9 (2016).
[68] B. Wysocki, J. Idaszek, J. Buhagiar, K. Szlązak, T. Brynk, K.J. Kurzydłowski, W. Święszkowski, Materials Science and Engineering: C, 95 (2019) 428-439.